Nano-Micro Letters

e-ISSN 2150-5551
CN 31-2103/TB

ARTICLE

https://doi.org/10.1007/s40820-022-00885-7

Cite as
Nano-Micro Lett.
(2022) 14:143

Received: 28 March 2022
Accepted: 30 May 2022
Published online: 9 July 2022

Tailoring Nitrogen Terminals on MXene Enables Fast Charging and Stable Cycling Na-Ion Batteries at Low Temperature

Yang Xia[1], Lanfang Que[2] ✉, Fuda Yu[2], Liang Deng[1], Zhenjin Liang[3], Yunshan Jiang[1], Meiyan Sun[1], Lei Zhao[1] ✉, Zhenbo Wang[1,4] ✉

HIGHLIGHTS

- An interlayer confined strategy to realize the substitution of nitrogen terminals between Ti_3C_2 MXene layers is proposed.
- The targeted Ti_3C_2-N_{funct} anode exhibits fast-charging ability and great superiority in cycle life at − 25 °C.
- Ti_3C_2-N_{funct} not only possesses a lower Na-ion diffusion energy barrier and charge transfer activation energy, but also exhibits Na^+-solvent co-intercalation behavior at low temperature.

ABSTRACT Sodium-ion batteries stand a chance of enabling fast charging ability and long lifespan while operating at low temperature (low-T). However, sluggish kinetics and aggravated dendrites present two major challenges for anodes to achieve the goal at low-T. Herein, we propose an interlayer confined strategy for tailoring nitrogen terminals on Ti_3C_2 MXene (Ti_3C_2-N_{funct}) to address these issues. The introduction of nitrogen terminals endows Ti_3C_2-N_{funct} with large interlayer space and charge redistribution, improved conductivity and sufficient adsorption sites for Na^+, which improves the possibility of Ti_3C_2 for accommodating more Na atoms, further enhancing the Na^+ storage capability of Ti_3C_2. As revealed, Ti_3C_2-N_{funct} not only possesses a lower Na-ion diffusion energy barrier and charge transfer activation energy, but also exhibits Na^+-solvent co-intercalation behavior to circumvent a high de-solvation energy barrier at low-T. Besides, the solid electrolyte interface dominated by inorganic compounds is more beneficial for the Na^+ transfer at the electrode/electrolyte interface. Compared with of the unmodified sample, Ti_3C_2-N_{funct} exhibits a twofold capacity (201 mAh g^{-1}), fast-charging ability (18 min at 80% capacity retention), and great superiority in cycle life (80.9%@5000 cycles) at − 25 °C. When coupling with $Na_3V_2(PO_4)_2F_3$ cathode, the Ti_3C_2-N_{funct}//NVPF exhibits high energy density and cycle stability at − 25 °C.

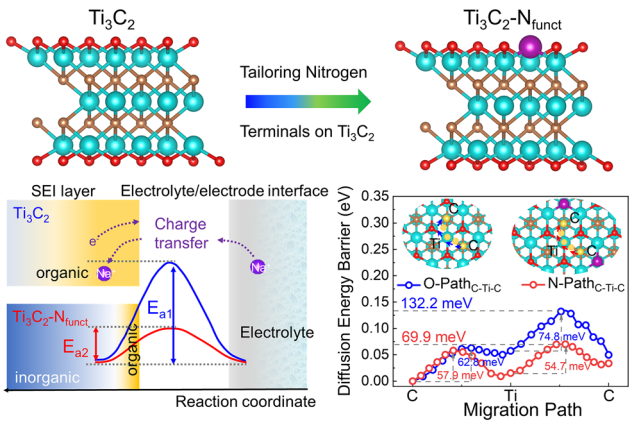

KEYWORDS Tailoring nitrogen terminals; Na^+-solvent co-intercalation; Interfacial kinetics; Fast charging; Low-temperature SIBs

✉ Lanfang Que, quelanfang@126.com; Lei Zhao, leizhao@hit.edu.cn; Zhenbo Wang, wangzhb@hit.edu.cn
[1] MIIT Key Laboratory of Critical Materials Technology for New Energy Conversion and Storage, State Key Lab of Urban Water Resources and Environment, School of Chemistry and Chemical Engineering, Harbin Institute of Technology, Harbin 150001, People's Republic of China
[2] Engineering Research Center of Environment-Friendly Functional Materials, Ministry of Education, Institute of Materials Physical Chemistry, Huaqiao University, Xiamen 361021, People's Republic of China
[3] The Institute for Advanced Studies, Wuhan University, Wuhan 430072, People's Republic of China
[4] College of Materials Science and Engineering, Shenzhen University, Shenzhen 518071, People's Republic of China

1 Introduction

The ever-increasing demand such as space exploration, military defence, and electric vehicles impels researchers to focus on developing high-performance energy storage devices at low temperature (low-T) [1–3]. Although great efforts have been made to improve the low-T performance, lithium-ion batteries (LIBs) cannot be charged at high currents at low-T and are accompanied by safety risks due to serious dendrite problems [4]. And these issues will be more prominent if commercial graphite is used as the anode. In this regard, researchers turn their attention to sodium-ion batteries (SIBs) owing to the low cost and superior temperature tolerance compared to LIBs [5]. In addition, the de-solvation energy of Na^+ is about 25–30% smaller than Li^+, meaning a lower activation barrier of Na (de) insertion [6], which is promising to achieve faster charging and higher battery performance at low-T according to the Arrhenius formula [7]. However, their low-T performance is still limited due to the subzero-temperature induced sluggish ionic transport in electrodes, decreased ions conductivity in electrolytes, and increased impedance between electrode and electrolyte [8, 9].

To solve these issues, external warming devices and self-heating systems are applied successively (Scheme 1a), which realize the low-T operation with minimal battery performance loss [10]. However, an extra high current is required for initial activation. Besides, the self-heating devices need to change the structure of the battery and lead to uneven heat distribution; thus there are certain safety risks [11]. Electrolytes are considered as a key reason for battery performance loss, due to the increased viscosity and poor ionic transport at low-T. Great efforts, such as employing low-melting-point solvents, high ions conductive electrolytes, novel salt additives and designing the solvation structure of electrolytes, are made to develop electrolytes applicable to low-T conditions [12–14]. Though several electrolytes (e.g., the mixture of PC and EC, ether-based electrolytes) have been found suitable for low-T operation, low-T batteries are still hindered by the slow charging process (Scheme 1b), if carbon-based anodes are employed [15, 16]. Serious polarization at high current density under low-T leads to the fast arrival of cut-off voltages, resulting in minimal accessible capacity and notorious dendrites formation. As proposed by the Sand time model, the time (τ) of the appearance of dendrites is

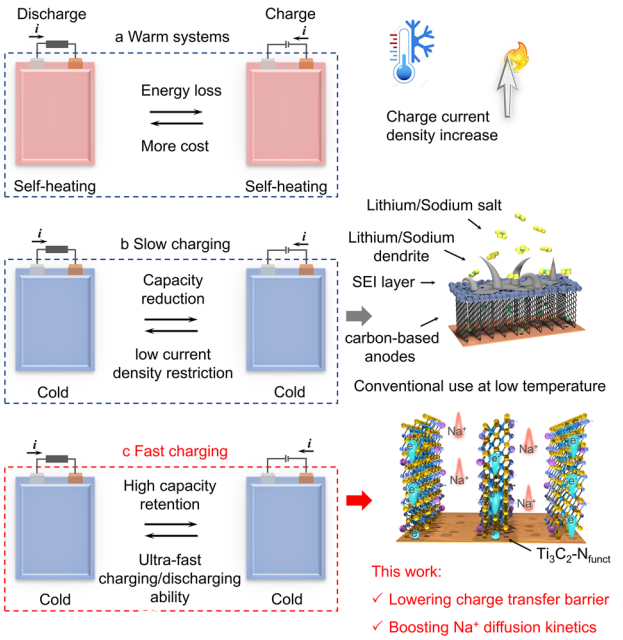

Scheme 1 Operational schemes of low-temperature Li/Na-ion batteries and the importance of constructing batteries with fast charging ability at low temperature. **a** Thermal management required during both charge and discharge processes. **b** Slowly charging required or cannot be charged at low temperature. **c** Batteries capable of both fast charging and cycle stability at low temperature

inversely proportional to the square of the current density (J) and directly proportional to ionic diffusion (D) [17–19].

$$\tau = \pi e^2 D\left(1 + \mu_c/\mu_a\right)^2 C_0^2/4J^2 \quad (1)$$

in which μ_c and μ_a are the mobilities of cation and anion, and C_0 is the initial concentration of the electrolyte. Therefore, it is vital to develop novel anode materials that possess fast interfacial kinetics to conquer these challenges at low-T.

Ti_3C_2, a typical member of the MXenes family, possessing high conductivity, large interlayer spacing, low Na^+ diffusion barrier, high theoretical capacity and appropriate operation voltage, is prospective anode material of SIBs at low-T [20, 21]. However, the surface terminations, such as –OH and –F, highly affect the electronic conductivity and adsorb ability of cations [22, 23]. Restacking of nanosheets causes poor electrolyte wettability and ion accessibility, leading to sluggish ion diffusion and limited reversible capacity [24, 25]. In general, the performance of MXenes has been improved at low-T by constructing 3D architectures to enhance ionic

https://doi.org/10.1007/s40820-022-00885-7

accessibility, interlayer pillaring and surficial groups regulation [9, 26–31]. Tailoring surficial terminals on MXenes is a method to improve the charge transfer process by directly regulating electronic structure [23, 32]. On the other hand, surficial terminals would promote interfacial chemical bonding between ions and substrates to suppress the formation of dendrites [33]. However, compared to the conventional gas doping methods, it is still a great challenge to find a facile and efficient strategy to tailor terminals between Ti_3C_2 MXene layers. Moreover, the ions storage mechanism of MXenes under low temperature is still rarely reported.

Herein, to lower the charge transfer barrier and boost ions diffusion kinetics, an interlayer confined strategy for tailoring nitrogen terminals on Ti_3C_2 has been proposed, which realizes the fast charging ability at − 25 °C (Scheme 1c). The pre-intercalated cetyltrimethylammonium bromide (CTAB) not only introduces nitrogen source into Ti_3C_2 MXene layers for designing nitrogen terminals (Ti_3C_2-N_{funct}), but also supports the layer structure during the annealing process. The corresponding structural transformation and formation mechanism are demonstrated by variable temperature in situ X-ray diffraction (XRD). As revealed by density functional theory (DFT) calculations, tailoring nitrogen terminals would lead to charge redistribution on Ti_3C_2 layer, narrowing the bandgap, endowing the sodiophilicity, and reducing the diffusion energy barrier. The comprehensive X-ray photoelectron spectroscopy (XPS) analyses indicate that the solid electrolyte interface (SEI) formed on the Ti_3C_2 and Ti_3C_2-N_{funct} electrode shows different composition changes with more inorganic compounds in the interior when formed on Ti_3C_2-N_{funct} electrode, which is essential for the Na^+ transfer at the electrode/electrolyte interface. In addition, the multi-scale physical characterizations show that Ti_3C_2-N_{funct} might possess Na^+-solvent co-intercalation behavior to circumvent the de-solvation process to achieve fast kinetics at low-T. Therefore, the designed Ti_3C_2-N_{funct} anodes deliver high reversible capacity, fast-charging ability, and superior cycling stability (80.9% after 5000 cycles) at − 25 °C. When coupling with $Na_3V_2(PO_4)_2F_3$ cathode, the full cells yield high energy density and high capacity retention at − 25 °C.

2 Results and Discussion

2.1 Preparation of Ti_3C_2-N_{funct} MXene

As depicted in Fig. S1, the Ti_3C_2-N_{funct} is realized by the in situ thermal decomposition of the pre-intercalated CTAB molecules between the interlayers of Ti_3C_2 (Ti_3C_2-$CT_{confined}$). First, the intercalation of CTAB and its effect on the layer structure of Ti_3C_2 is proved and analysed. The electrostatic interaction between negative-charged surface of Ti_3C_2 and the positive-charged CTAB impels Ti_3C_2 sheets to expand to accommodate CTAB, which guarantees the intercalation of nitrogen source in layers of Ti_3C_2 [34–38]. Fourier transform infrared spectroscopy (FTIR) spectra demonstrate that the peaks corresponding to R_4N^+ and -CH_2 stretching modes of cetyltrimethylammonium (CTA^+) shift to a lower wave in Ti_3C_2-$CT_{confined}$, implying the electrostatic interaction between CTAB and Ti_3C_2 (Fig. 1a). XRD patterns exhibit that the (002) peak of Ti_3C_2-$CT_{confined}$ become wider and shift to a lower angle compared to Ti_3C_2 (Fig. S2). This is completely different from the simple overlaying of (002) peak and CTAB peak observed in Ti_3C_2-CT_{mix} (Ti_3C_2 physically mixed with CTAB powders), further verifying that CTAB has successfully intercalated in the layers of Ti_3C_2. Such a phenomenon is consistent with high-resolution transmission electron microscopy (HRTEM) images, wherein the interlayer spacing of Ti_3C_2 enlarges to 1.45 nm from 1.13 nm after CTAB pre-intercalation (Fig. 1e, f). Second, the interlayered confined CTAB will decompose and part of the released N atoms will be captured by Ti_3C_2 to form nitrogen terminals during the annealing process. Temperature is a crucial factor that strongly influence the formation of surface terminations on MXenes. To determine the optimal tailoring temperature, in situ high-temperature XRD and thermogravimetric analysis (TGA) were performed to track the thermal structural transformation of Ti_3C_2-$CT_{confined}$ as demonstrated in Figs. 1b and S3. When the temperature rises from 25 to 200 °C, the (002) peak of Ti_3C_2-$CT_{confined}$ slightly shifts to a higher angle, and a weight loss of 2.2% is observed both in Ti_3C_2 and Ti_3C_2-$CT_{confined}$, which could

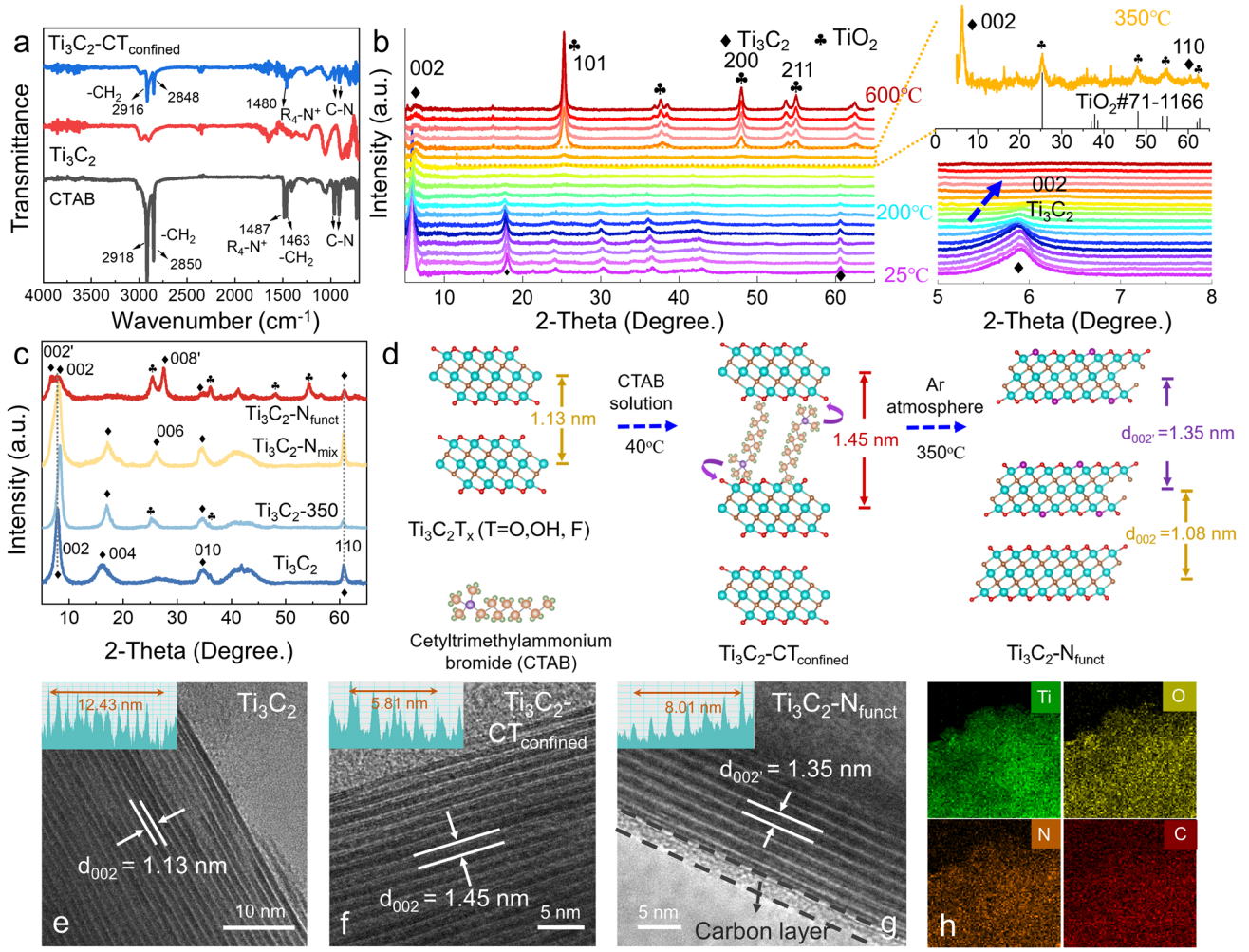

Fig. 1 **a** FTIR spectra of CTAB powder, Ti_3C_2 and Ti_3C_2-$CT_{confined}$. **b** In situ high-temperature XRD patterns, enlarged view within 5°–8° of Ti_3C_2-$CT_{confined}$ within 25–600 °C, and enlarged view of XRD pattern at 350 °C. **c** XRD patterns of Ti_3C_2, Ti_3C_2-350, Ti_3C_2-N_{mix} and Ti_3C_2-N_{funct}. **d** Illustration of Ti_3C_2 during the tailoring process. HRTEM images of **e** Ti_3C_2, **f** Ti_3C_2-$CT_{confined}$ and **g** Ti_3C_2-Nfunct. **h** Ti, O, N, and C elements mappings of Ti_3C_2-N_{funct}

be ascribed to the loss of water adsorbed in the layers of Ti_3C_2 [39]. The salient deviation of TGA curves from 200 to 250 °C between Ti_3C_2 and Ti_3C_2-$CT_{confined}$ can be attributed to the decomposition of CTAB, in which N atoms are released from CTAB (Fig. S3). With the temperature increasing above 300 °C, the removal of surficial terminals will take place as in previous reports [29, 40]. When the temperature rises to 350 °C, there is an obvious drop in the TGA curves of Ti_3C_2-$CT_{confined}$ compared to Ti_3C_2 and pure CTAB powder. Such a phenomenon could be attributed to the low carbonization ratio of CTAB and the confined effect of MXene on CTAB. A new peak is gradually formed at 25.2° (Fig. 1b), which belongs to anatase TiO_2 (JCPDS No. 71-1166) [41]. However, the (002) and (110) peaks belonging to Ti_3C_2 are still maintained, implying the layer structure could be kept at 350 °C. When temperature keeps rising, the intensity of (002) peak decreases and more characteristic peaks of anatase TiO_2 appear, confirming that Ti_3C_2 would inevitably transform to anatase TiO_2 at a higher temperature. To confirm the tailoring temperature, the electrochemical performance of Ti_3C_2-$CT_{confined}$ annealing between 300 and 400 °C were compared, as shown in Fig. S4. Due to the low tailoring efficiency under 300 °C and serious oxidation of Ti_3C_2 under 400 °C, 350 °C is considered as an appropriate temperature for tailoring nitrogen terminals on Ti_3C_2.

https://doi.org/10.1007/s40820-022-00885-7

To illustrate the important role of CTAB pre-intercalation in the preparation of Ti_3C_2-N_{funct}, XRD patterns of Ti_3C_2-N_{funct}, Ti_3C_2-N_{mix} (product of Ti_3C_2-CT_{mix} after annealing at 350 °C), Ti_3C_2-350 (Ti_3C_2 powder after annealing at 350 °C), and Ti_3C_2 are compared (Fig. 1c). The main diffraction peaks of Ti_3C_2-N_{mix} are similar to that of Ti_3C_2 and the peak of anatase TiO_2 is also observed in Ti_3C_2-350. Moreover, a thick carbon layer on Ti_3C_2-N_{mix} also indicated that CTAB decomposed outside of Ti_3C_2 layers (Fig. S5). Since the introduction of CTAB, more TiO_2 peaks are observed in Ti_3C_2-N_{funct} than in other samples. The split-up of (002) peak in Ti_3C_2-N_{funct} further indicates that Ti_3C_2-N_{funct} still keeps large interlayer spacing after the decomposition of pillared CTAB. This is consistent well with the TEM images shown in Fig. 1e–g, wherein Ti_3C_2 shows a layer distance of 1.13 nm and expands to 1.45 nm after the CTAB intercalation, then reduces to 1.35 nm after thermal treatment. Figure 1d illustrates the structure evolution of Ti_3C_2 during the preparation of Ti_3C_2-N_{funct} and the phenomenon of (002) peak splitting. Moreover, the N element is distributed uniformly on Ti_3C_2-N_{funct} (Fig. 1h). The crinkled nanosheets remain after thermal treatment (Fig. S6), ensuring electrolyte wettability and ion accessibility. These results demonstrate that CTAB pre-intercalation and thermal treatment can achieve uniform N doping and make Ti_3C_2-N_{funct} maintain well-layered structure with a large lattice distance, while the physical mixing of CTAB cannot achieve this effect.

2.2 Electronic Structure Analysis

XPS was applied to record the difference of the valence states of Ti/O elements and the existence of N between Ti_3C_2-$CT_{confined}$ and Ti_3C_2-N_{funct}. The Ti 2*p* spectra of Ti_3C_2-$CT_{confined}$, Ti_3C_2-N_{funct}, and Ti_3C_2 are provided in Figs. 2a and S7a, a new peak appears at 456.5 eV, which is attributed to Ti-N in Ti_3C_2-N_{funct}, indicating that N atoms bond with Ti atoms on Ti_3C_2 [42–44]. Moreover, the O 1*s* spectra reflect the change of surficial composition on Ti_3C_2 (Fig. 2b) [45, 46]. The peak at 533.8 eV, corresponding to -ON derived from the electrostatic interaction between N atoms in CTAB and surficial O-terminals of Ti_3C_2, disappears in Ti_3C_2-N_{funct}. In addition, the C-Ti peak of Ti_3C_2, Ti_3C_2-$CT_{confined}$ and Ti_3C_2-N_{funct} also reflect the electrostatic interaction between CTAB and Ti_3C_2 (Fig. S7). Different from the existence of lattice substitution for C atoms (396.0 eV) in previous reports, the N 1*s* peak can only be split into two peaks located at 399.8 and 402.0 eV in this work, corresponding to the surficial N-terminals and adsorbed N atoms, labelled as N_{funct} and N_{ads} (Fig. 2c) [32, 42]. It is clear that, after the thermal treatment, the proportion of N_{funct} increases sharply, further verifying the successful transformation of adsorbed N atoms in CTAB to the bonding N atoms in Ti_3C_2-N_{funct}. The concentrations of nitrogen element in Ti_3C_2-$CT_{confined}$ and Ti_3C_2-N_{funct} are 3.63 and 1.05 at%, as exhibited in Table S1.

DFT calculation was conducted to figure out the effect of tailoring N-terminals on the electronic structure of Ti_3C_2. A $3\times2\times1$ supercell of $Ti_3C_2O_2$ is constructed as the initial structure as demonstrated in Fig. S8a. An oxygen atom is substituted by a nitrogen atom in the supercell to approximate the N atoms concentration in Ti_3C_2-N_{funct} (Fig. S8b), corresponding to a chemical stoichiometry of $Ti_3C_2O_{1.83}N_{0.17}$. Charge accumulation around N atoms and depletion near Ti atoms are verified by electron density difference (EDD) in Fig. 2d. Based on Eq. 2, the plane-averaged EDD $\Delta\rho$ and the charge transfer ΔQ are delivered to quantitatively compare the charge discrepancy after N substitution (Fig. 2d right) [8]. It could be observed that more charge will transfer from N atoms to Ti atoms compared to that of O atoms. The Mulliken charge distribution demonstrates that Ti atoms bond with N atoms and inner Ti atoms obtain more electrons with a reduced charge (Fig. 2d). These results are consistent with Ti 2*p* XPS spectra in Fig. 2a, in which the peaks of Ti-C and Ti^{2+}-C slightly shift to low binding energy due to more electrons provided by N atoms. The above observations suggest that the N- terminals could induce a charge redistribution, leading to the formation of more active sites of redox reactions [44].

$$\Delta Q(z) = \int \Delta\rho\left(z'\right)\mathrm{d}z' \tag{2}$$

The density of states (DOS) of $Ti_3C_2O_2$ and $Ti_3C_2O_{1.83}N_{0.17}$ are shown in Fig. 2e. As observed, the conduction band (CB) of $Ti_3C_2O_2$ and $Ti_3C_2O_{1.83}N_{0.17}$ is mainly contributed by Ti 3*d*, while the valence band (VB) originates from the hybridization of Ti 3*d*, C 2*p* and O 2*p* [32]. The bandgap is reduced from 0.15 to 0.13 eV after N atom substitution, manifesting that electrons could easily migrate from VB to CB, implying the enhanced electronic conductivity of $Ti_3C_2O_{1.83}N_{0.17}$. The DOS shape of $Ti_3C_2O_{1.83}N_{0.17}$

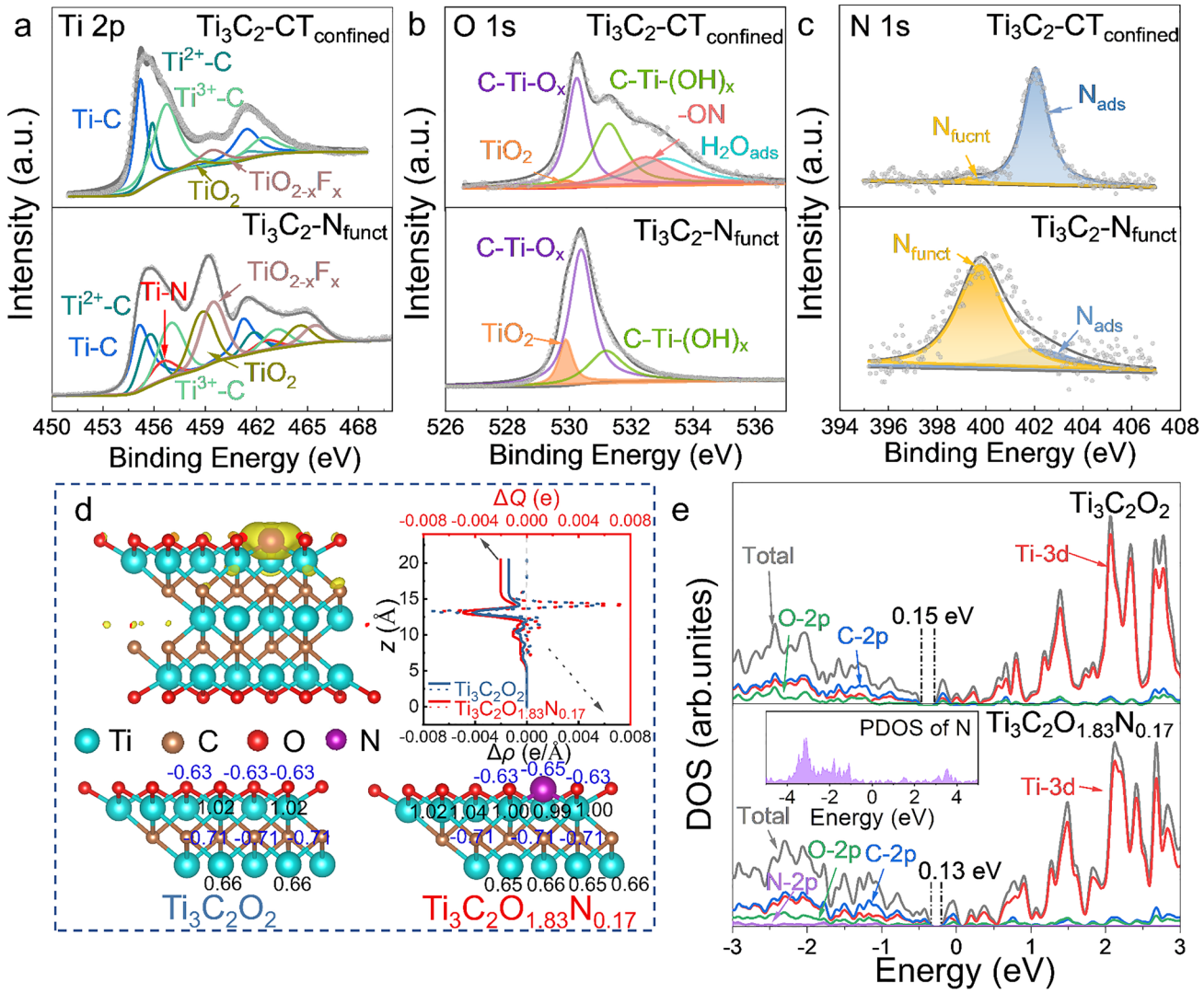

Fig. 2 High-resolution XPS spectra of **a** Ti 2*p*, **b** O 1*s*, and **c** N 1*s* of Ti_3C_2-$CT_{confined}$ and Ti_3C_2-N_{funct}. **d** Electron density difference (EDD) of $Ti_3C_2O_{1.83}N_{0.17}$, in which yellow is positive; the line-profiles of plane-averaged EDD $\Delta\rho$ (dot line) and amount of transferred charge ΔQ (solid line); the atomic populations of $Ti_3C_2O_2$ and $Ti_3C_2O_{1.83}N_{0.17}$. **e** The calculated density of states (DOS) and partial density of states (PDOS) of $Ti_3C_2O_2$ and $Ti_3C_2O_{1.83}N_{0.17}$

below the Fermi level is sharper, indicating that the substitution of N atoms makes electrons more localized [47], which is beneficial for the chemical bonding with Na^+ to increase the driving force for nucleation to inhibit the formation of metallic Na nuclei [33]. Such improvement is particularly important at low temperatures and can effectively inhibit the formation of sodium dendrites to achieve fast charging ability. This speculation will be confirmed in the next part.

Furthermore, the adsorption energy of Na atom on $Ti_3C_2O_2$ and $Ti_3C_2O_{1.83}N_{0.17}$ is investigated to demonstrate the sodiophilicity of N-groups on Ti_3C_2. The optimized geometric structures of a Na atom on monolayer $Ti_3C_2O_2$ and $Ti_3C_2O_{1.83}N_{0.17}$ are exhibited in Figs. S9 and S10. As exhibited in Fig. S11, after tailoring N-terminals on Ti_3C_2, the adsorption energy becomes more negative, confirming the adsorption stability of Na. It is worthy to notice that the adsorption sites near the N atoms possess the lowest adsorption energy among types of C top and Ti top, suggesting that the surficial N-terminals would induce Na^+ to form a Na–N–Ti interaction to keep the lowest energy state. Such a phenomenon indicates that the existence of N-terminal on Ti_3C_2 could regulate the Na deposition behavior. Moreover,

 https://doi.org/10.1007/s40820-022-00885-7

the optimized structures of a Na atom intercalating in double layers of $Ti_3C_2O_2$ and $Ti_3C_2O_{1.83}N_{0.17}$ are exhibited in Fig. S12, wherein the $Ti_3C_2O_{1.83}N_{0.17}$ possesses larger interlayer spacing, in accordance with HRTEM results (Fig. 1 g). The negative formation energy suggests that Na^+ prefers to intercalate into the layers of Ti_3C_2. The result suggests that the surficial nitrogen terminals regulation could effectively improve the electronic conductivity, enhancing the sodiophilicity of Ti_3C_2, and improve the possibility of Ti_3C_2 for accommodating more Na atoms, further enhancing the Na^+ storage capability of Ti_3C_2.

2.3 Electrochemical Performance at − 25 °C

Based on the well-tailored Ti_3C_2-N_{funct} anode, half-cells are assembled with metallic Na to evaluate the electrochemical performance at − 25 °C. Ti_3C_2-N_{funct} delivers a much higher capacity, which is nearly 2 times that of Ti_3C_2 at 25 and − 25 °C (Fig. 3a). Besides, the capacity loss caused by the temperature drop is greatly reduced, and the reversible capacity of Ti_3C_2-N_{funct} at − 25 °C is about 77% of room temperature. The first charging/discharging curves of Ti_3C_2 and Ti_3C_2-N_{funct} demonstrate that SEI forms in the first discharge process, which leads to the unpleasant initial Coulombic efficiency (Fig. S13). Figure 3b is the rate capability of the two anodes at − 25 °C, the specific capacities of Ti_3C_2-N_{funct} are 201, 182, 172, 160, 143, 126, and 90 mAh g^{-1} at 0.05, 0.1, 0.2, 0.5, 1.0, 2.0, and 5.0 A g^{-1}, while about half of the capacity is obtained in Ti_3C_2. The Ti_3C_2-N_{funct} anode delivers fast-charging/discharging ability at low-T, which could recharge to 80% capacity (160 mAh g^{-1}) within 18 min and 72% capacity (144 mAh g^{-1}) in 8 min (Fig. S14). After 5000 cycles at 1.0 A g^{-1} at − 25 °C, the Ti_3C_2-N_{funct} electrode maintains capacity retention of 80.9% (Fig. 3d), superior to most reported low-T batteries as shown in Table S2 and Fig. 3c [48–50].

In addition, $Na_3V_2(PO_4)_2F_3$ cathode, due to its high capacity retention and reversibility of Na^+ at low-T [51], was selected as the basis of eventual full-cell construction (Fig. 3g). The electrochemical performance of $Na_3V_2(PO_4)_2F_3$ cathodes are shown in Fig. S15. The

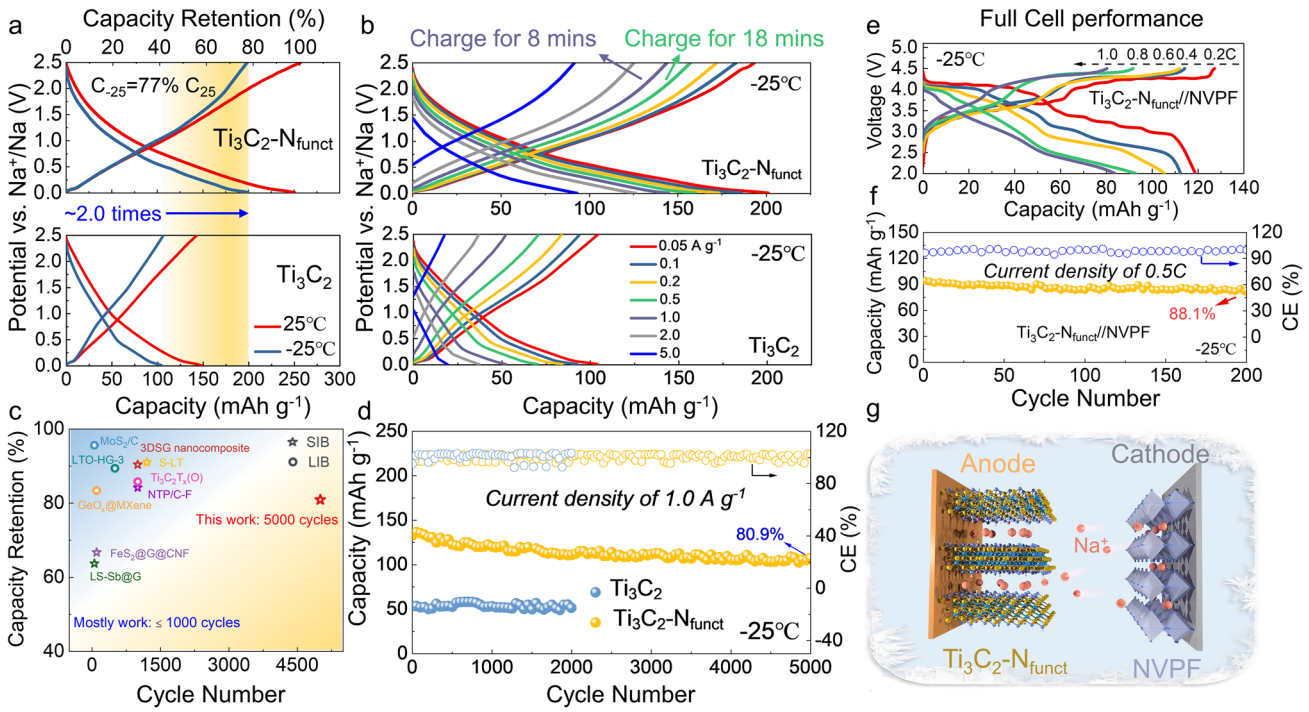

Fig. 3 Electrochemical performance of Ti_3C_2 and Ti_3C_2-N_{funct} anodes in Na-ion half-cells and Ti_3C_2-N_{funct}//NVPF full-cell. **a** The second charge/discharge curves of Ti_3C_2 and Ti_3C_2-N_{funct} anodes in Na-ion half-cells at 0.05 A g^{-1} under 25 and − 25 °C. **b** Rate capabilities of half-cells at − 25 °C. **c** Comparison of low-T cycle performance of Ti_3C_2-N_{funct} vs. other reported LIBs and SIBs. **d** Cycle performance of half cell at − 25 °C. **e** Rate performance (1C represents 0.128 mA g^{-1}) and **f** cycling stability at 0.5C of Ti_3C_2-N_{funct}//NVPF full-cell. **g** Illustration of Ti_3C_2-N_{funct}//NVPF full-cell

reversible capacities of 118 mAh g^{-1} (based on the mass of cathode material) at 0.2C have been achieved (1C represents 0.128 mA g^{-1}), which keeps high capacity retention (95%) compared to room temperature (Figs. 3e and S16). The designed Ti_3C_2-N_{funct}//NVPF SIB displays excellent cycle stability at − 25 °C (Fig. 3f), which keeps capacity retention of 88.1% after 200 cycles at 0.5C. Moreover, as shown in Fig. S17, the Ti_3C_2-N_{funct}//NVPF full cell achieves a maximum energy density and power density of 414.14 Wh kg^{-1} and 763.98 W kg^{-1} at − 25 °C, respectively (based on the cathode material). Hence, the interlayer confined strategy for tailoring N-terminals on Ti_3C_2 is effective for improving the Na^+ storage performance at low-T of MXenes including temperature adaptability, fast-charging ability, and ultra-long lifespan.

2.4 Analysis of Kinetics of Ti_3C_2-N_{funct} Anode at Low Temperature

Given a deeper insight into the effects of tailoring N-terminals on Ti_3C_2, DFT calculations and various experimental analyses were delivered to investigate the kinetics of Ti_3C_2 and Ti_3C_2-N_{funct}. To clarify the fast diffusion process of Na^+ in Ti_3C_2-N_{funct}, DFT calculations of energy barrier of possible Na^+ diffusion paths in bilayer framework for $Ti_3C_2O_2$ and $Ti_3C_2O_{1.83}N_{0.17}$ were carried out. As previous results in Fig. S11, the site on top of C atoms is preferred Na adsorption sites. Therefore, two possible pathways of Na^+ between the two nearest neighboring C sites in the bilayer of $Ti_3C_2O_2$ are explored (Fig. 4a). For O-$Path_{C\text{-}C}$, the Na^+ is hopping directly to the nearest C site in a one-step path; for O-$Path_{C\text{-}Ti\text{-}C}$, the Na^+ is migrating along the pathway from the top of C atoms to the top of Ti atoms and then to the nearest C atoms [22, 52]. The calculated energy barrier of two paths are 288.7 and 132.2 meV, indicating that Na^+ tends to migrate along the $path_{C\text{-}Ti\text{-}C}$. When an oxygen atom is substituted by a nitrogen atom in $Ti_3C_2O_{1.83}N_{0.17}$, C atoms with different chemical environment are emerging, labelled as C^A, C^B, C^C, and C^D. Therefore, three diffusion directions of Na^+ in the bilayer of $Ti_3C_2O_{1.83}N_{0.17}$ are explored as shown in Figs. 4b, c and S18–S19. It is noteworthy that the diffusion energy barrier of $path_{C\text{-}Ti\text{-}C}$ in $Ti_3C_2O_{1.83}N_{0.17}$ is lower than that of $Ti_3C_2O_2$ and the energy barrier for Na^+ hopping over the Ti-N bonds is lower than that of Ti–O bonds, demonstrating that tailoring N-terminals on Ti_3C_2 is efficient to facilitate Na^+ diffusion. Especially, the N-$Path_C{}^A{}_{\text{-}Ti}{}^1{}_{\text{-}C}{}^B$ for Na^+ migration is presented in Fig. 4b, with a calculated energy barrier as low as 69.9 meV, which is much lower than that of typical Na-ion insertion materials as previous reported, such as TiO_2 (2.20 eV), TiS_2 (1.20 eV), and $TiSe_2$ (0.5 eV), confirming the fast kinetics of Ti_3C_2-N_{funct} [53–55].

The Na^+ storage behavior of Ti_3C_2-N_{funct} electrodes at − 25 °C is verified by the cyclic voltammetry (CV) curves at various scan rates from 0.2 to 2.0 mV s^{-1} (Fig. S20a). According to Eq. 3:

$$i = av^b \tag{3}$$

in which the Na^+ storage mechanisms can be defined as faradic ion intercalation ($b = 0.5$) or capacitive response ($b = 1.0$) [56]. The calculated b values for peak C_1, C_2, A_1, and A_2 are 0.89, 0.95, 0.88, and 0.94, respectively, demonstrating that the Ti_3C_2-N_{funct} electrodes possess fast kinetics at − 25 °C (Fig. S20b). The Na^+ diffusion coefficients and polarization of Ti_3C_2 and Ti_3C_2-N_{funct} electrodes at − 25 °C were identified by the galvanostatic intermittent titration technique (GITT) (Fig. 4d, details in Fig. S21). The Ti_3C_2-N_{funct} delivers much lower polarization during the charge/discharge process than that of Ti_3C_2 at − 25 °C, which might suppress the nucleation rate of Na dendrites as shown in Fig. 4e [18]. The calculated Na^+ diffusion coefficients of Ti_3C_2 and Ti_3C_2-N_{funct} electrodes at 25 and − 25 °C are demonstrated in Fig. 4f. At room temperature, the Na^+ diffusion coefficients of Ti_3C_2 and Ti_3C_2-N_{funct} are very close. However, while transferred to − 25 °C, Ti_3C_2-N_{funct} could nearly maintain the same Na^+ diffusion coefficients at room temperature, which is much higher than that of Ti_3C_2, indicating the better adaptability of Ti_3C_2-N_{funct} at low-T. This discrepancy is significant, as proposed by the Sand time model [17], the nearly 5.6 times difference in Na^+ diffusion coefficients is expected to prolong the time (τ) of dendrites appearing, which could guarantee the cycle stability at low-T. Therefore, beneficial from the interfacial chemical bonding of Na^+ and the low nucleation rate of Na dendrites, the Ti_3C_2-N_{funct} delivers excellent cycle stability.

The interfacial charge transfer dominates battery performance at low-T as previous studies reported, the activation energy (E_a) holds the key to determining the interfacial kinetics [7]. Based on the Butler–Volmer equation and Arrhenius equation, the relationship between charge transfer resistance (R_{ct}) and E_a is generalized as:

$$T/R_{ct} = A \exp\left(-E_a/RT\right) \tag{4}$$

https://doi.org/10.1007/s40820-022-00885-7

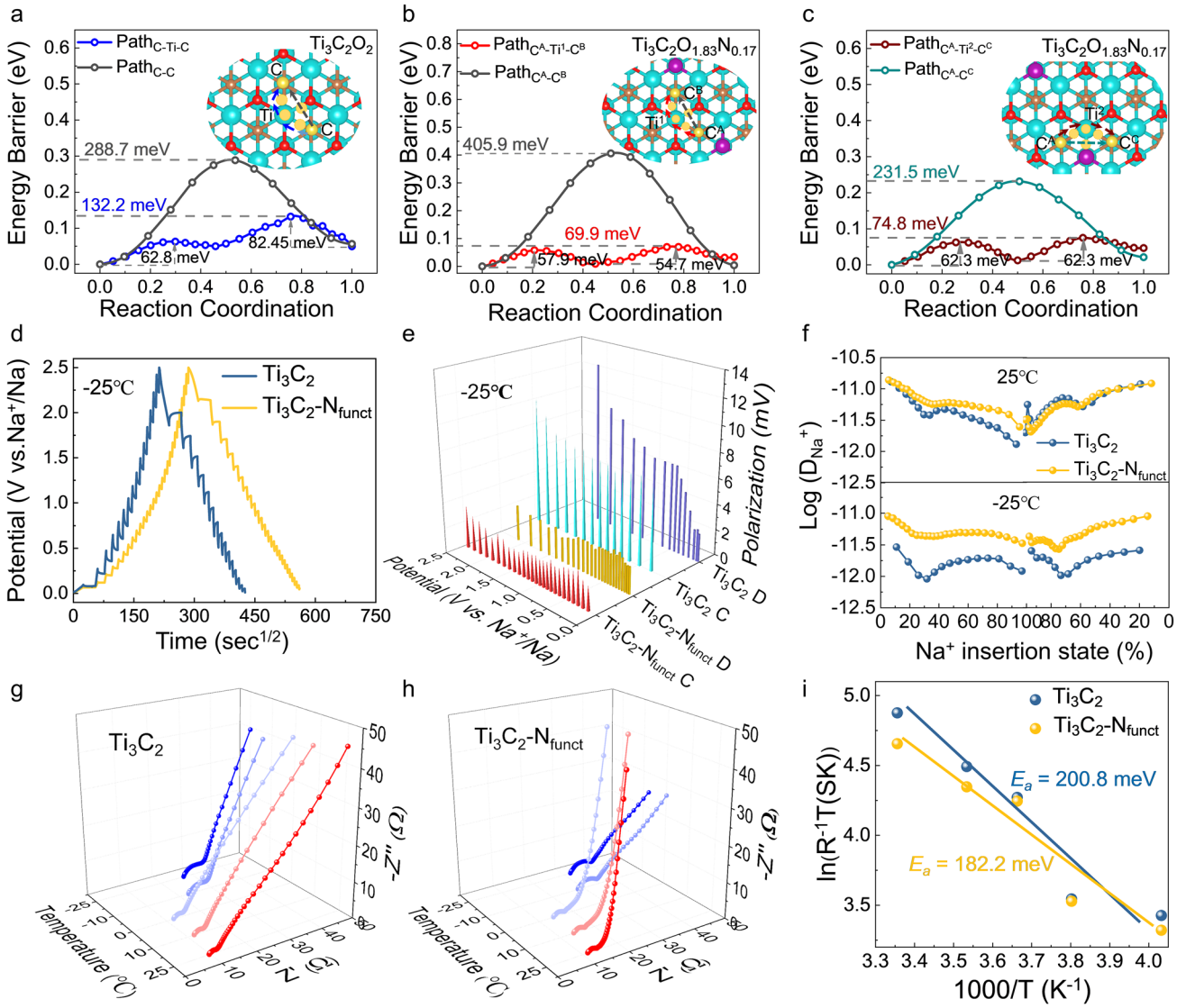

Fig. 4 Kinetics analysis: the diffusion energy barrier of Na^+ along different paths in **a** $Ti_3C_2O_2$ and **b-c** $Ti_3C_2O_{1.83}N_{0.17}$. **d** Charge–discharge GITT curves of Ti_3C_2 and Ti_3C_2-N_{funct}. **e** Comparison of polarization of the two electrodes at − 25 °C during the charge/discharge process. **f** The Na^+ diffusion coefficients of Ti_3C_2 and Ti_3C_2-N_{funct} at 25 °C and − 25 °C. Temperature-dependent EIS study of **g** Ti_3C_2 and **h** Ti_3C_2-N_{funct} anodes from − 25 to 25 °C. **i** Arrhenius plot of the resistance contributions of the charge transfer resistance (R_{ct}) with the derived activation energies (E_a) for the two electrodes

in which A is a constant, R is the gas constant, T is the temperature. As shown in Fig. 4g-h, the temperature-dependent EIS was performed to measure the value of R_{ct} from − 25 to 25 °C for Ti_3C_2 and Ti_3C_2-N_{funct} electrodes. The equivalent circuit model of Ti_3C_2 and Ti_3C_2-N_{funct} electrodes is exhibited in Fig. S22. The fitted R_{ct} values of Ti_3C_2 and Ti_3C_2-N_{funct} electrodes at various temperatures are exhibited in Table S3. It is noteworthy that the R_{ct} values of two electrodes are low, indicating the fast charge transfer process at − 25 °C. Based on Eq. 4, the calculated values of E_a for Ti_3C_2 and Ti_3C_2-N_{funct} electrodes are 200.8 and 182.2 meV (Fig. 4i), respectively. This result demonstrates that Ti_3C_2-N_{funct} could serve a nearly 10% reduction in activation energy during the interfacial charge transfer process than that of Ti_3C_2. All these observations further confirm that tailoring N-terminals on Ti_3C_2 not only accelerate interfacial kinetics and Na^+ diffusion but also lower the charge transfer energy barrier, which is essential for achieving fast-charging ability at low-T.

2.5 Analysis of Electrode/Electrolyte Interface

SEI is a crucial composition on electrode surface to affect the ion transport, which determines the electrochemical performance at low-T. To get deep insight of the SEI composition, high-resolution XPS of C 1*s*, O 1*s*, F 1*s*, and Na 1*s* spectra were collected from the electrode surface and in-depth of 10 nm with Ar^+ sputtering for both Ti_3C_2 and Ti_3C_2-N_{funct} anodes (after discharging to 0.01 V at − 25 °C), as shown in Figs. 5a–c and S23. The C 1*s* spectra are fitted using peaks with binding energies of 284.2 (C–Ti), 284.8 (C–C), 285.6 (C–O), 286.3 (CH_2–CF_2), 287.4 (C=O), 288.3 (RCH_2–F), 289.5 (O–C=O), and 290.8 (–CF_2–) eV, which are consistent with Ti_3C_2, the main reduction products of diglyme solvent, Na_2CO_3 and PVDF [57]. These are also corresponding to the peaks located at 530.6 (C–Ti–O_x), 531.0 (Na_2CO_3), 531.7 (C–Ti–$(OH)_x$), 532.6 (R–O–Na), and 533.8 (C=O) eV (Fig. 5b). Due to the reduction of TiO_2, the peak at 529.6 eV (Na–O–Ti) belonging to Na_xTiO_2 could be observed in O 1*s* spectra of Ti_3C_2-N_{funct} [58]. The peak located at 685.0 eV in F 1*s* spectra representing Na-F bond and the Na 1*s* spectra shows a peak at 1072.2 eV (Na–F and Na–O), demonstrating the existence of sodium compounds (Figs. 5c and S23) [51, 59]. Note that, the peak at 686.0 eV in F 1*s* spectra is belonging to the complex fluorosulfate, which is decomposed from $NaCF_3SO_3$ salt. Such a phenomenon could also be observed in the S 2*p* spectra (Figs. 5d and S24). Therefore, it can be inferred that the SEI layers formed on Ti_3C_2 and Ti_3C_2-N_{funct} anodes are composed of both organic compounds (RCH_2ONa and $ROCO_2Na$) and inorganic compounds (NaF and Na_2CO_3). The complex fluorosulfate is distributed near the surface of Ti_3C_2 electrode. It is noteworthy that there is a difference between SEI formed on the two electrodes, where the organic compounds are the main components in the SEI of Ti_3C_2 electrode and the inorganic compounds are dominated in the SEI of Ti_3C_2-N_{funct} electrode.

The compositions of SEI layer vary during the charge–discharge process. Figures 5e, f and S25 demonstrate the elemental compositions of SEI at different states of charge (SOC) and depths of Ti_3C_2 and Ti_3C_2-N_{funct} anodes. For both electrodes, the C and F concentrations decrease during the discharge process and increase when charging back to 2.5 V, while the trends of the O and Na concentrations are opposite. It could be ascribed to the formation and reconstruction of SEI layer during the discharge and charge process. Moreover, there is a difference between Ti_3C_2 and Ti_3C_2-N_{funct} electrodes when discharging to 0.01 V. For the Ti_3C_2-N_{funct} electrode, the C concentration decreases sharply with sputtering depths increasing, while the Na concentration increases and the O concentration decreases slightly. This phenomenon indicates that there is a thin organic compounds layer distributed near the surface and the inorganic compounds dominate the interior of the SEI. In contrast, there is no obvious change of the C and Na concentrations in the SEI of the Ti_3C_2 electrode. This means the organic compounds are distributed homogeneously in the SEI on the Ti_3C_2 electrode. Beneficial from the low charge transfer resistance of inorganic compounds as reported [58], the Ti_3C_2-N_{funct} electrode delivers lower activation energy during the interfacial charge transfer process as illustrated in Fig. 5g, which is consistent with the above dynamic analysis.

Moreover, the Ti 2*p* spectra of Ti_3C_2 and Ti_3C_2-N_{funct} at different SOC after Ar^+ etching to a depth of 10 nm are shown in Fig. 5d. The Ti 2*p* spectra of Ti_3C_2-N_{funct} have greatly changed after discharged to 0.01 V, wherein the ratio of Ti^{2+}-C increases and the peaks of Ti^{2+}-C, Ti^{3+}-C, and Ti-N shift to the lower binding energy, indicating the reduced valence of Ti and the formation of Ti–O–Na and Na–N–Ti interaction [60]. After the extraction of Na^+, the partial Ti^{2+} is oxidized to Ti^{3+} when charged back to 2.5 V, demonstrating the reversible redox reactions of the Ti^{3+}/Ti^{2+} couple. However, as for the Ti_3C_2 electrode, the ratio of Ti^{2+}-C and Ti^{3+}-C in Ti 2*p* spectra nearly maintained during the discharging and charging process. Such a phenomenon demonstrates that tailoring N-terminals on Ti_3C_2 provides more active sites for the redox reaction and induces more charge transfer during the charge/discharge process, leading to higher capacity. Overall, due to the inorganic component of SEI layer and more active sites for redox reaction, it is easy to understand the reason why Ti_3C_2-N_{funct} delivers better sodium storage performance than that of Ti_3C_2 as shown in Fig. 3.

2.6 Na^+ Storage Mechanism of Ti_3C_2-N_{funct} at Low Temperature

How do Ti_3C_2-N_{funct} participate in the electrochemical reactions at low-T? Cycling performance is used to compare the Na^+ storage capability of Ti_3C_2-N_{funct} at different conditions (Fig. 6c). Interestingly, Ti_3C_2-N_{funct} electrode delivers stable

 https://doi.org/10.1007/s40820-022-00885-7

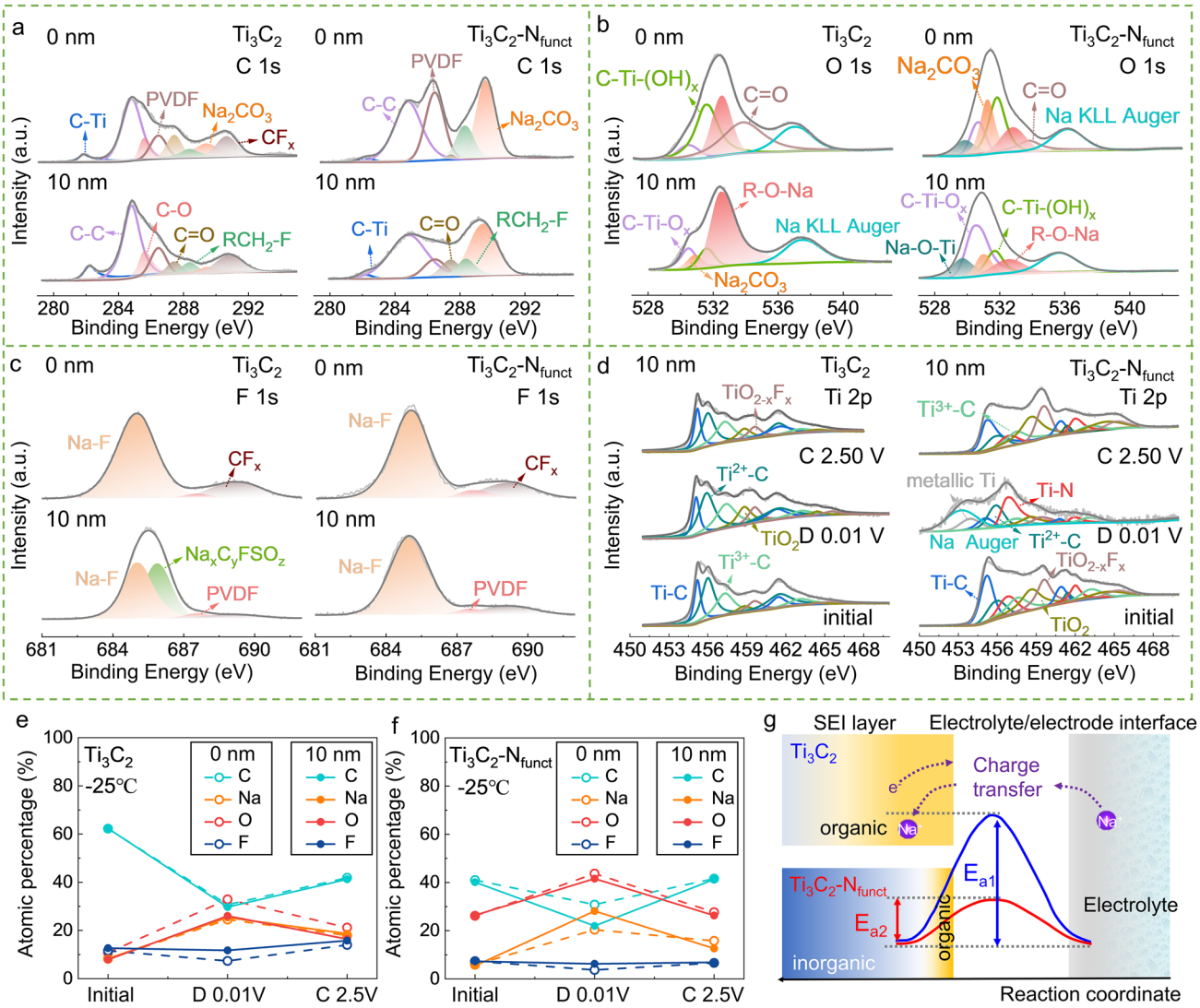

Fig. 5 The surface composition analysis of Ti_3C_2 and Ti_3C_2-N_{funct} electrodes operating at −25 °C by XPS etching. XPS **a** C 1*s*, **b** O 1*s* and **c** F 1*s* spectra of the Ti_3C_2 and Ti_3C_2-N_{funct} electrodes after first discharging to 0.01 V. **d** Ti 2*p* spectra for Ti_3C_2 and Ti_3C_2-N_{funct} at different states of charge (SOC) after Ar^+ etching of 10 nm. The atomic percentage of C, Na, O, F of **e** Ti_3C_2 and **f** Ti_3C_2-N_{funct} electrodes at different SOC. **g** Illustration of the SEI compositions formed on Ti_3C_2 and Ti_3C_2-N_{funct} electrodes and a comparison of the charge transfer energy barriers

cycling performance at − 25 °C than that at room temperature. To facilitate a deep understanding of the sodiation behavior of Ti_3C_2-N_{funct}, in situ and ex situ XRD measurements were made to demonstrate the structure reversibility during the charging–discharging process under different conditions. In situ XRD patterns with 2θ ranging from 6.0° to 9.0° and 22.5°–27.5° of Ti_3C_2-N_{funct} operating at room temperature are displayed in Fig. 6a. According to the discharge curve, the sodiation process can be divided into surficial adsorption and intercalation. Although the (002) peak belonging to Ti_3C_2 fixes at 8.3° during the continuous discharging–charging process, the (002′) peak shifts to a higher angle during discharging, and then could not return when get the fully charged state. Moreover, the (008') peak disappears during discharging and reemerges at the charged state, which could be attributed to the intercalation of Na^+. These intercalated Na^+ will attract the MXene layers to each other, leading to a reduced interlayer space [61, 62]. The

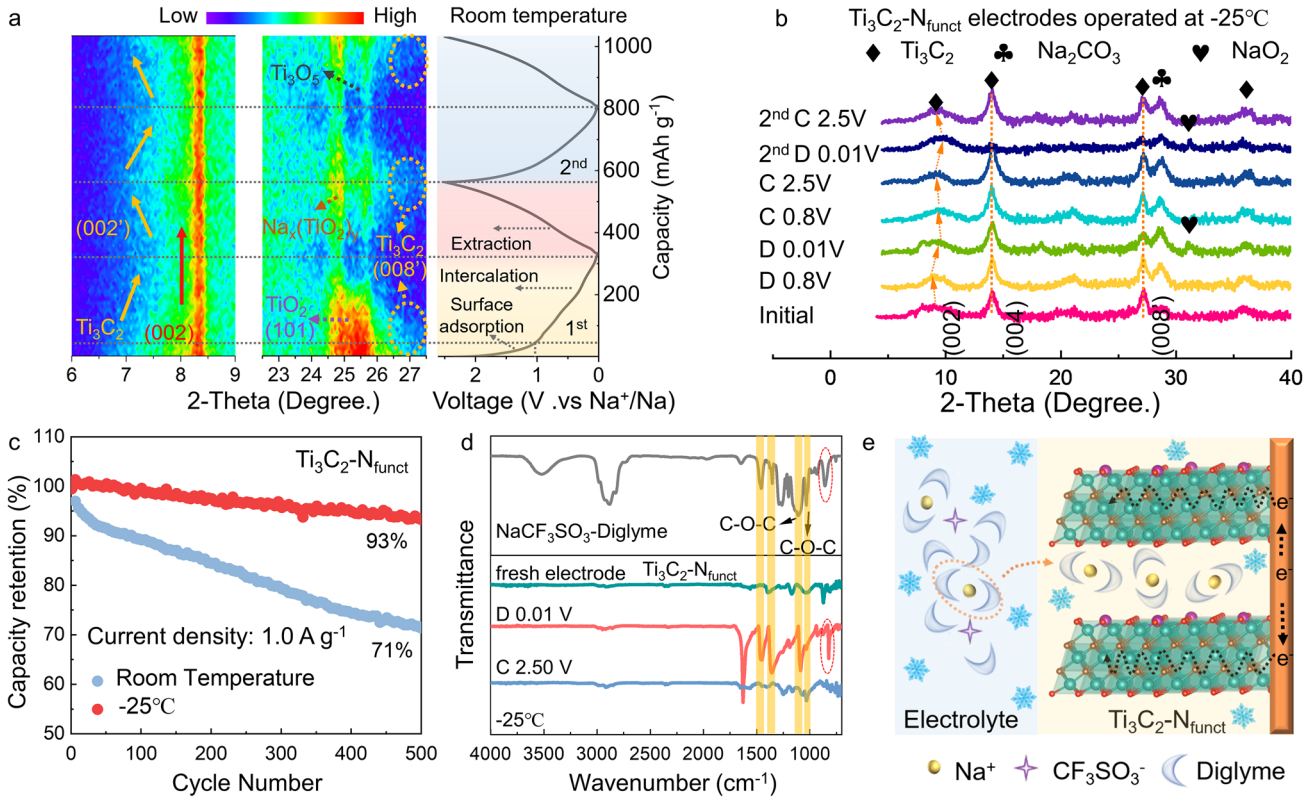

Fig. 6 **a** In situ XRD patterns of Ti_3C_2-N_{funct} operating at room temperature with 2θ ranging from 6.0° to 9.0° and 22.5°–27.5°, the first two charge/discharge curves corresponding to the in situ XRD patterns. **b** Ex situ XRD patterns of Ti_3C_2-N_{funct} electrodes operating at − 25 °C. **c** Comparison of cycling performance for Ti_3C_2-N_{funct} operating at room temperature and − 25 °C. **d** Ex situ FTIR spectra of Ti_3C_2-N_{funct} electrodes. **e** Illustration of Na^+-solvent co-intercalation behavior in Ti_3C_2-N_{funct} at low-T

obvious variation for the layer structure of Ti_3C_2-N_{funct} during the charging–discharging process would lead to unstable cycling performance at room temperature. The reflections located between 22.5° and 27.5° are attributed to the sodiation process of TiO_2, in which TiO_2 is transformed to sodium titanates (JCPDS No. 78-1590), titanium suboxide (JCPDS No. 72-2101) [58]. However, the TiO_2 particles forming during the tailoring process didn't contribute to the increased capacity of Ti_3C_2-N_{funct} as shown in Fig. S26. In addition, TiO_2-N_{mix} (deriving from the annealing product of TiO_2 mixed with CTAB powders) exhibits an unpleasant performance than pure TiO_2, further proving that the improved performance of Ti_3C_2-N_{funct} exactly stemmed from tailoring surficial N-terminals rather than the contribution of TiO_2 (Fig. S27).

To explore the Na^+ storage mechanism at low-T, ex situ XRD patterns of Ti_3C_2-N_{funct} electrodes operating at − 25 °C were recorded (Fig. 6b). Interestingly, after aging for 1 h in Na-ion half-cell at − 25 °C, the potential of Ti_3C_2-N_{funct} reduced 0.05 V (Fig. S28a). It could be attributed to the chemical pre-sodiation of Ti_3C_2-N_{funct} during the aging process, leading to the broaden of (002) peak, the shift of (004) peak of Ti_3C_2-N_{funct}, and the disappearance of peaks of anatase TiO_2 (Fig. S28b). It has been reported that the anatase TiO_2 would transform into amorphous structure when sodiated at low temperature [63]. The widened (002) peak shifts to a lower angle when firstly discharged to 0.8 V, and then it returns to the higher angle at the fully discharged state. Two new lattice peaks are detected at 28.5° and 31.4°, corresponding to Na_2CO_3 and NaO_2. Different from operating at room temperature, the interlayer spacing of Ti_3C_2-N_{funct} is enlarged before discharging to 0.8 V, and then it shrinks during subsequent discharging process at low-T. Such phenomenon could be correlated to the intercalation of the solvent molecules [61, 64]. Moreover, the slight the variation of (002) peak indicates the stable structure of

 https://doi.org/10.1007/s40820-022-00885-7

Ti_3C_2-N_{funct}, leading to outstanding cycling performance at low-T. The elemental mapping of Ti_3C_2-N_{funct} at a deep-discharged state is exhibited in Fig. S29 further prove the Na^+ intercalation at low-T.

It is believed that the desolvation process is the rate-determining step at low-T due to the high desolvation energy barrier [65, 66]. As previous studies have indicated that there is an ion–solvent co-intercalation behavior in graphitic structure when operated in the ether-based electrolytes with high solvation energy [67, 68], we speculate that the graphite-like MXenes possessing larger interlayer spacing might deliver the similar ion–solvent co-intercalation behavior to circumvent the desolvation process to achieve fast kinetics at low-T. To confirm the hypothesis, the ex situ FTIR spectra of Ti_3C_2-N_{funct} electrodes during sodiation and desodiation are collected. The FTIR spectra of the electrolyte (1 M $NaCF_3SO_3$ in diglyme) and pure solvent (diglyme) are compared in Fig. S30, demonstrating that the peak at 858 cm^{-1} belonging to the solvated Na^+ [69]. The characteristic peaks of the solvated Na^+ appear at the full discharged state and disappear when charged back to 2.5 V in the ex situ FTIR spectra of Ti_3C_2-N_{funct} and Ti_3C_2 (Figs. 6d and S31). Our previous work shows that if the solvent is simply adsorbed on the surface of the material, its signal is independent of the state of charge and could be detected during the whole charging–discharging process [70]. In Ti_3C_2-N_{funct}, the characteristic peaks of diglyme solvent are strongly associated with SOC, suggesting that Na^+ and solvent might possess similar migration behavior. Therefore, integrating these evidences into account, we deduced that Ti_3C_2-N_{funct} possesses Na^+-solvent co-intercalation behavior during the charge transfer process as illustrated in Fig. 6e, which could avoid the high desolvation energy barrier to realize the fast-charging ability at low-T.

3 Conclusions

In summary, we propose and demonstrate that tailoring nitrogen terminals on Ti_3C_2 through the interlayer confined strategy is crucial to enable high-performance SIBs at low temperature. N atoms derived from the decomposition of confined CTAB molecules directly substitute the surface terminals, which tailor the in-plane structure of Ti_3C_2. The interfacial kinetics and energy storage mechanism at − 25 °C of Ti_3C_2-N_{funct} are investigated. It is found that tailoring nitrogen terminals could boost Na^+ diffusion kinetics and lower charge transfer barrier by the synergistic effects of large interlayer spacing, charge redistribution, and strong adsorption, empowering Ti_3C_2-N_{funct} with higher Na^+ diffusion coefficient and a 10% reduction in activation energy at low-T. The inorganic compounds in the SEI on Ti_3C_2-N_{funct} are beneficial for Na^+ transfer. Moreover, the ion–solvent co-intercalation behavior endows Ti_3C_2-N_{funct} with fast-charging ability at low-T. As expected, the Ti_3C_2-N_{funct} anodes deliver high capacity retention, fast-charging ability (charging 80% capacity within 18 min), and ultra-long lifespan (5000 cycles with a capacity retention of 80.9%) at − 25 °C, far exceeding that of pristine Ti_3C_2. The assembled Ti_3C_2-N_{funct}//NVPF full cells also deliver high energy density and cycling stability at − 25 °C. This work opens avenues for the development of other 2D materials in constructing high-energy storage systems at low temperatures.

Acknowledgements We acknowledge the National Natural Science Foundation of China (Grant Nos. 21673064, 51902072 and 22109033), Heilongjiang Touyan Team (Grant No. HITTY-20190033), Fundamental Research Funds for the Central Universities (Grant Nos. HIT. NSRIF. 2019040 and 2019041), State Key Laboratory of Urban Water Resource and Environment (Harbin Institute of Technology) (Grant No. 2020 DX11). We acknowledge the support of the High-Performance Computing Center (HPCC) at Harbin Institute of Technology on first-principles calculations.

Funding Open access funding provided by Shanghai Jiao Tong University.

Supplementary Information The online version contains supplementary material available at https://doi.org/10.1007/s40820-022-00885-7.

References

1. A. Gupta, A. Manthiram, Designing advanced lithium-based batteries for low-temperature conditions. Adv. Energy Mater. **10**(38), 2001972 (2020). https://doi.org/10.1002/aenm.202001972
2. X. Dong, Z.W. Guo, Z.Y. Guo, Y. Wang, Y. Xia, Organic batteries operated at −70°C. Joule **2**(5), 902–913 (2018). https://doi.org/10.1016/j.joule.2018.01.017
3. Y. Liu, Y. Zhu, Y. Cui, Challenges and opportunities towards fast-charging battery materials. Nat. Energy **4**(7), 540–550 (2019). https://doi.org/10.1038/s41560-019-0405-3
4. M.J. Lee, K. Lee, J. Lim, M. Li, S. Noda et al., Outstanding low-temperature performance of structure-controlled graphene anode based on surface-controlled charge storage mechanism. Adv. Funct. Mater. **31**(14), 2009397 (2021). https://doi.org/10.1002/adfm.202009397
5. J. Deng, W.B. Luo, S.L. Chou, H.K. Liu, S.X. Dou, Sodium-ion batteries: from academic research to practical commercialization. Adv. Energy Mater. **8**(4), 1701428 (2018). https://doi.org/10.1002/aenm.201701428
6. T. Hosaka, K. Kubota, A.S. Hameed, S. Komaba, Research development on K-ion batteries. Chem. Rev. **120**(14), 6358–6466 (2020). https://doi.org/10.1021/acs.chemrev.9b00463
7. W. Zhang, X. Sun, Y. Tang, H. Xia, Y. Zeng et al., Lowering charge transfer barrier of $LiMn_2O_4$ via nickel surface doping to enhance Li^+ intercalation kinetics at subzero temperatures. J. Am. Chem. Soc. **141**(36), 14038–14042 (2019). https://doi.org/10.1021/jacs.9b05531
8. L.F. Que, F.D. Yu, Y. Xia, L. Deng, K. Goh et al., Enhancing Na-ion storage at subzero temperature via interlayer confinement of Sn^{2+}. ACS Nano **14**(10), 13765–13774 (2020). https://doi.org/10.1021/acsnano.0c05925
9. X. Gao, X. Du, T.S. Mathis, M.M. Zhang, X.H. Wang et al., Maximizing ion accessibility in MXene-knotted carbon nanotube composite electrodes for high-rate electrochemical energy storage. Nat. Commun. **11**, 6160 (2020). https://doi.org/10.1038/s41467-020-19992-3
10. C.Y. Wang, G.S. Zhang, S.H. Ge, T. Xu, Y. Ji et al., Lithium-ion battery structure that self-heats at low temperatures. Nature **529**(7587), 515–518 (2016). https://doi.org/10.1038/nature16502
11. X.S. Hu, Y.S. Zheng, D.A. Howey, H. Perez, A. Foley et al., Battery warm-up methodologies at subzero temperatures for automotive applications: recent advances and perspectives. Prog. Energy Combust. Sci. **77**, 100806 (2020). https://doi.org/10.1016/j.pecs.2019.100806
12. J. Holoubek, H.D. Liu, Z.H. Wu, Y.J. Yin, X. Xing et al., Tailoring electrolyte solvation for Li metal batteries cycled at ultra-low temperature. Nat. Energy **6**, 303–313 (2021). https://doi.org/10.1038/s41560-021-00783-z
13. B. Liao, H.Y. Li, M.Q. Xu, L.D. Xing, Y.H. Liao et al., Designing low impedance interface films simultaneously on anode and cathode for high energy batteries. Adv. Energy Mater. **8**(22), 1800802 (2018). https://doi.org/10.1002/aenm.201800802
14. M.C. Smart, B.L. Lucht, S. Dalavi, F.C. Krause, B.V. Ratnakumar, The effect of additives upon the performance of MCMB/$LiNi_xCo_{1-x}O_2$ Li-ion cells containing methyl butyrate-based wide operating temperature range electrolytes. J. Electrochem. Soc. **159**(6), A739–A751 (2012). https://doi.org/10.1149/2.058206jes
15. Z.H. Lin, Q.B. Xia, W.L. Wang, W.S. Li, S.L. Chou, Recent research progresses in ether- and ester-based electrolytes for sodium-ion batteries. InfoMat **1**(3), 376–389 (2019). https://doi.org/10.1002/inf2.12023
16. Y.X. Huang, L.Z. Zhao, L. Li, M. Xie, F. Wu et al., Electrolytes and electrolyte/electrode interfaces in sodium-ion batteries: from scientific research to practical application. Adv. Mater. **31**(21), 1808393 (2019). https://doi.org/10.1002/adma.201808393
17. C. Brissot, M. Rosso, J.N. Chazalviel, P. Baudry, S. Lascaud, In-situ study of dendritic growth in lithium/PEO-salt/lithium cells. Electrochim. Acta **43**, 1569–1574 (1998). https://doi.org/10.1016/S0013-4686(97)10055-X
18. B. Lee, E. Paek, D. Mitlin, S.W. Lee, Sodium metal anodes: emerging solutions to dendrite growth. Chem. Rev. **119**(8), 5416–5460 (2019). https://doi.org/10.1021/acs.chemrev.8b00642
19. Y. Zhang, T.T. Zuo, J. Popovic, K. Lim, Y.X. Yin et al., Towards better Li metal anodes: challenges and strategies. Mater. Today **33**, 56–74 (2020). https://doi.org/10.1016/j.mattod.2019.09.018
20. D. Er, J. Li, M. Naguib, Y. Gogotsi, V.B. Shenoy, Ti_3C_2 MXene as a high capacity electrode material for metal (Li, Na, K, Ca) ion batteries. ACS Appl. Mater. Interfaces **6**(14), 11173–11179 (2014). https://doi.org/10.1021/am501144q
21. P. Ma, D. Fang, Y. Liu, Y. Shang, Y. Shi et al., MXene-based materials for electrochemical sodium-ion storage. Adv. Sci. **8**(11), 2003185 (2021). https://doi.org/10.1002/advs.202003185
22. Q. Tang, Z. Zhou, P. Shen, Are MXenes promising anode materials for Li ion batteries? Computational studies on electronic properties and Li storage capability of Ti_3C_2 and $Ti_3C_2X_2$ (X = F, OH) monolayer. J. Am. Chem. Soc. **134**(40), 16909–16916 (2012). https://doi.org/10.1021/ja308463r
23. Y. Xie, M. Naguib, V.N. Mochalin, M.W. Barsoum, Y. Gogotsi et al., Role of surface structure on Li-ion energy storage capacity of two-dimensional transition-metal carbides. J. Am. Chem. Soc. **136**(17), 6385–6394 (2014). https://doi.org/10.1021/ja501520b
24. M.Q. Zhao, X. Xie, C.E. Ren, T. Makaryan, B. Anasori et al., Hollow MXene spheres and 3D macroporous MXene frameworks for Na-ion storage. Adv. Mater. **29**(37), 1702410 (2017). https://doi.org/10.1002/adma.201702410
25. F. Song, J. Hu, G. Li, J. Wang, S. Chen et al., Room-temperature assembled MXene-based aerogels for high mass-loading sodium-ion storage. Nano-Micro Lett. **14**, 37 (2021). https://doi.org/10.1007/s40820-021-00781-6
26. N. Zhao, F. Zhang, F. Zhan, D. Yi, Y. Yang et al., Fe^{3+}-stabilized Ti_3C_2T MXene enables ultrastable Li-ion

 https://doi.org/10.1007/s40820-022-00885-7

storage at low temperature. J. Mater. Sci. Technol. **67**, 156–164 (2021). https://doi.org/10.1016/j.jmst.2020.06.037

27. X. Wang, J. Wang, J. Qin, X. Xie, R. Yang et al., Surface charge engineering for covalently assembling three-dimensional MXene network for all-climate sodium ion batteries. ACS Appl. Mater. Interfaces **12**(35), 39181–39194 (2020). https://doi.org/10.1021/acsami.0c10605
28. Y. Wu, P. Nie, L. Wu, H. Dou, X. Zhang, 2D MXene/SnS_2 composites as high-performance anodes for sodium ion batteries. Chem. Eng. J. **334**, 932–938 (2018). https://doi.org/10.1016/j.cej.2017.10.007
29. Y. Wang, C. Ma, W. Ma, W. Fan, Y. Sun et al., Enhanced low-temperature Li-ion storage in MXene titanium carbide by surface oxygen termination. 2D Mater. **6**(4), 045025 (2019). https://doi.org/10.1088/2053-1583/ab30f9
30. N. Sun, Z. Guan, Q. Zhu, B. Anasori, Y. Gogotsi et al., Enhanced ionic accessibility of flexible MXene electrodes produced by natural sedimentation. Nano-Micro Lett. **12**, 89 (2020). https://doi.org/10.1007/s40820-020-00426-0
31. P. Zhang, R. Soomro, Z. Guan, N. Sun, B. Xu, 3D carbon-coated MXene architectures with high and ultrafast lithium/sodium-ion storage. Energy Storage Mater. **29**, 163–171 (2020). https://doi.org/10.1016/j.ensm.2020.04.016
32. C. Lu, L. Yang, B. Yan, L. Sun, P. Zhang et al., Nitrogen-doped Ti_3C_2 MXene: mechanism investigation and electrochemical analysis. Adv. Funct. Mater. **30**(47), 2000852 (2020). https://doi.org/10.1002/adfm.202000852
33. J. Zheng, D.C. Bock, T. Tang, Q. Zhao, J. Yin et al., Regulating electrodeposition morphology in high-capacity aluminium and zinc battery anodes using interfacial metal-substrate bonding. Nat. Energy **6**(4), 398–406 (2021). https://doi.org/10.1038/s41560-021-00797-7
34. J. Luo, W. Zhang, H. Yuan, C. Jin, L. Zhang et al., Pillared structure design of mxene with ultralarge interlayer spacing for high-performance lithium-ion capacitors. ACS Nano **11**(3), 2459–2469 (2017). https://doi.org/10.1021/acsnano.6b07668
35. J. Luo, J. Zheng, J. Nai, C. Jin, H. Yuan et al., Atomic sulfur covalently engineered interlayers of Ti_3C_2 MXene for ultrafast sodium-ion storage by enhanced pseudocapacitance. Adv. Funct. Mater. **29**(10), 1808107 (2019). https://doi.org/10.1002/adfm.201808107
36. J. Zhang, Q. Lei, Z. Ren, X. Zhu, J. Li et al., A superlattice-stabilized layered CuS anode for high-performance aqueous zinc-ion batteries. ACS Nano **15**, 17748–17756 (2021). https://doi.org/10.1021/acsnano.1c05725
37. F. Zhang, X. Guo, P. Xiong, J. Zhang, J. Song et al., Interface engineering of MXene composite separator for high-performance Li-Se and Na-Se batteries. Adv. Energy Mater. **10**(20), 2000446 (2020). https://doi.org/10.1002/aenm.202000446
38. J. Luo, X. Lu, E. Matios, C. Wang, H. Wang et al., Tunable MXene-derived 1D/2D hybrid nanoarchitectures as a stable matrix for dendrite-free and ultrahigh capacity sodium metal anode. Nano Lett. **20**(10), 7700–7708 (2020). https://doi.org/10.1021/acs.nanolett.0c03215
39. O. Mashtalir, M. Naguib, V.N. Mochalin, Y. Dall'Agnese, M. Heon et al., Intercalation and delamination of layered carbides and carbonitrides. Nat. Commun. **4**, 1716 (2013). https://doi.org/10.1038/ncomms2664
40. J. Hart, K. Hantanasirisakul, A. Lang, B. Anasori, D. Pinto et al., Control of MXenes' electronic properties through termination and intercalation. Nat. Commun. **10**, 522 (2019). https://doi.org/10.1038/s41467-018-08169-8
41. P. Wang, X. Lu, Y. Boyjoo, X. Wei, Y. Zhang et al., Pillar-free TiO_2/Ti_3C_2 composite with expanded interlayer spacing for high-capacity sodium ion batteries. J. Power Sources **451**, 227756 (2020). https://doi.org/10.1016/j.jpowsour.2020.227756
42. W. Bao, L. Liu, C. Wang, S. Choi, D. Wang et al., Facile synthesis of crumpled nitrogen-doped MXene nanosheets as a new sulfur host for lithium-sulfur batteries. Adv. Energy Mater. **8**(13), 1702485 (2018). https://doi.org/10.1002/aenm.201702485
43. Y. Wen, T.E. Rufford, X. Chen, N. Li, M. Lyu et al., Nitrogen-doped $Ti_3C_2T_x$ MXene electrodes for high-performance supercapacitors. Nano Energy **38**, 368–376 (2017). https://doi.org/10.1016/j.nanoen.2017.06.009
44. N. Chen, Y. Zhou, S. Zhang, H. Huang, C. Zhang et al., Tailoring Ti_3CNT_x MXene via an acid molecular scissor. Nano Energy **85**, 106007 (2021). https://doi.org/10.1016/j.nanoen.2021.106007
45. J. Halim, K.M. Cook, M. Naguib, P. Eklund, Y. Gogotsi et al., X-ray photoelectron spectroscopy of select multi-layered transition metal carbides (MXenes). Appl. Surf. Sci. **362**, 406–417 (2016). https://doi.org/10.1016/j.apsusc.2015.11.089
46. Y. Tian, W. Que, Y. Luo, C. Yang, X. Yin et al., Surface nitrogen-modified 2D titanium carbide (MXene) with high energy density for aqueous supercapacitor applications. J. Mater. Chem. A **7**(10), 5416–5425 (2019). https://doi.org/10.1039/c9ta00076c
47. Y. Zhou, F. Che, M. Liu, C. Zou, Z. Liang et al., Dopant-induced electron localization drives CO_2 reduction to C_2 hydrocarbons. Nat. Chem. **10**(9), 974–980 (2018). https://doi.org/10.1038/s41557-018-0092-x
48. X. Rui, X. Zhang, S. Xu, H. Tan, Y. Jiang et al., A low-temperature sodium-ion full battery: superb kinetics and cycling stability. Adv. Funct. Mater. **31**(11), 2009458 (2020). https://doi.org/10.1002/adfm.202009458
49. Y.Y. Wang, B.H. Hou, J.Z. Guo, Q.L. Ning, W.L. Pang et al., An ultralong lifespan and low-temperature workable sodium-ion full battery for stationary energy storage. Adv. Energy Mater. **8**(18), 1703252 (2018). https://doi.org/10.1002/aenm.201703252
50. C. Chen, Y. Yang, X. Tang, R. Qiu, S. Wang et al., Graphene-encapsulated FeS_2 in carbon fibers as high reversible anodes for Na^+ /K^+ batteries in a wide temperature range. Small **15**(10), 1804740 (2019). https://doi.org/10.1002/smll.201804740
51. L. Deng, K. Goh, F.D. Yu, Y. Xia, Y.S. Jiang et al., Self-optimizing weak solvation effects achieving faster low-temperature charge transfer kinetics for high-voltage $Na_3V_2(PO_4)_2F_3$ cathode. Energy Storage Mater. **44**, 82–92 (2022). https://doi.org/10.1016/j.ensm.2021.10.012

52. X. Wang, X. Shen, Y. Gao, Z. Wang, R. Yu et al., Atomic-scale recognition of surface structure and intercalation mechanism of Ti_3C_2X. J. Am. Chem. Soc. **137**(7), 2715–2721 (2015). https://doi.org/10.1021/ja512820k
53. R. Zheng, H. Yu, X. Zhang, Y. Ding, M. Xia et al., A $TiSe_2$-graphite dual ion battery: fast Na-ion insertion and excellent stability. Angew. Chem. Int. Ed. **60**(34), 18430–18437 (2021). https://doi.org/10.1002/anie.202105439
54. C. Chen, Y. Wen, X. Hu, X. Ji, M. Yan et al., Na^+ intercalation pseudocapacitance in graphene-coupled titanium oxide enabling ultra-fast sodium storage and long-term cycling. Nat. Commun. **6**, 6929 (2015). https://doi.org/10.1038/ncomms7929
55. T. Liu, X. Zhang, M. Xia, H. Yu, N. Peng et al., Functional cation defects engineering in TiS_2 for high-stability anode. Nano Energy **67**, 104295 (2020). https://doi.org/10.1016/j.nanoen.2019.104295
56. L.F. Que, F.D. Yu, X.L. Sui, L. Zhao, J.G. Zhou et al., Thermal-induced interlayer defect engineering toward super high-performance sodium ion capacitors. Nano Energy **59**, 17–25 (2019). https://doi.org/10.1016/j.nanoen.2019.02.030
57. N. Schulz, R. Hausbrand, C. Wittich, L. Dimesso, W. Jaegermann, XPS-surface analysis of SEI layers on Li-ion cathodes: part II. SEI-composition and formation inside composite electrodes. J. Electrochem. Soc. **165**(5), A833–A846 (2018). https://doi.org/10.1149/2.0881803jes
58. K. Li, J. Zhang, D. Lin, D.W. Wang, B. Li et al., Evolution of the electrochemical interface in sodium ion batteries with ether electrolytes. Nat. Commun. **10**, 725 (2019). https://doi.org/10.1038/s41467-019-08506-5
59. Z. Tang, H. Wang, P.F. Wu, S.Y. Zhou, Y.C. Huang et al., Electrode-electrolyte interfacial chemistry modulation for ultra-high rate sodium-ion battery. Angew. Chem. Int. Ed. **61**(18), e202200475 (2022). https://doi.org/10.1002/anie.202200475
60. J. Luo, C. Fang, C. Jin, H. Yuan, O. Sheng et al., Tunable pseudocapacitance storage of MXene by cation pillaring for high performance sodium-ion capacitors. J. Mater. Chem. A **6**(17), 7794–7806 (2018). https://doi.org/10.1039/c8ta02068j
61. X. Wang, T.S. Mathis, K. Li, Z. Lin, L. Vlcek et al., Influences from solvents on charge storage in titanium carbide MXenes. Nat. Energy **4**(3), 241–248 (2019). https://doi.org/10.1038/s41560-019-0339-9
62. M. Okubo, A. Sugahara, S. Kajiyama, A. Yamada, MXene as a charge storage host. Acc. Chem. Res. **51**(3), 591–599 (2018). https://doi.org/10.1021/acs.accounts.7b00481
63. D. Lin, K. Li, Q. Wang, L. Lyu, B. Li et al., Rate-independent and ultra-stable low-temperature sodium storage in pseudocapacitive TiO_2 nanowires. J. Mater. Chem. A **7**(33), 19297–19304 (2019). https://doi.org/10.1039/c9ta05039f
64. S. Kajiyama, L. Szabova, K. Sodeyama, H. Iinuma, R. Morita et al., Sodium-ion intercalation mechanism in MXene nanosheets. ACS Nano **10**(3), 3334–3341 (2016). https://doi.org/10.1021/acsnano.5b06958
65. J. Holoubek, Y. Yin, M. Li, M. Yu, Y.S. Meng et al., Exploiting mechanistic solvation kinetics for dual-graphite batteries with high power output at extremely low temperature. Angew. Chem. Int. Ed. **58**(52), 18892–18897 (2019). https://doi.org/10.1002/anie.201912167
66. J. Chen, Y. Peng, Y. Yin, Z. Fang, Y. Cao et al., A desolvation-free sodium dual-ion chemistry for high power density and extremely low temperature. Angew. Chem. Int. Ed. **60**(44), 23858–23862 (2021). https://doi.org/10.1002/anie.202110501
67. M. Liu, L. Xing, K. Xu, H. Zhou, J. Lan et al., Deciphering the paradox between the co-intercalation of sodium-solvent into graphite and its irreversible capacity. Energy Storage Mater. **26**, 32–39 (2020). https://doi.org/10.1016/j.ensm.2019.12.026
68. M.L. Divya, Y.S. Lee, V. Aravindan, Solvent co-intercalation: an emerging mechanism in Li-, Na-, and K-ion capacitors. ACS Energy Lett. **6**(12), 4228–4244 (2021). https://doi.org/10.1021/acsenergylett.1c01801
69. Z. Li, Y. Zhang, J. Zhang, Y. Cao, J. Chen et al., Sodium-ion battery with a wide operation-temperature range from -70 to 100°C. Angew. Chem. Int. Ed. **61**, e202116930 (2022). https://doi.org/10.1002/anie.202116930
70. M.Y. Sun, F.D. Yu, Y. Xia, L. Deng, Y.S. Jiang et al., Trigger Na^+-solvent co-intercalation to achieve high-performance sodium-ion batteries at subzero temperature. Chem. Eng. J. **430**, 132750 (2022). https://doi.org/10.1016/j.cej.2021.132750

 https://doi.org/10.1007/s40820-022-00885-7